



# Ablation characteristics on silicon from ultrafast laser radiation containing single MHz and GHz burst pulses

Daniel Metzner<sup>1,2</sup> · Peter Lickschat<sup>1</sup> · Andy Engel<sup>1</sup> · Thomas Lampke<sup>2</sup> · Steffen Weißmantel<sup>1</sup>

Received: 29 April 2022 / Accepted: 7 July 2022 / Published online: 30 July 2022  
© The Author(s) 2022

## Abstract

The authors present results of ablation on silicon with ultrafast laser radiation featuring burst pulses using an amplified burst-mode solid-state laser, featuring an emitting wavelength of 1030 nm to generate single burst cavities on silicon. Laser parameter are varied for different pulse durations from 270 fs up to 10 ps, burst fluences, and number of sub-pulses per burst in the respective burst regime with sub-pulse repetition rates of 65 MHz and 5 GHz. The resulting ablated volume per burst and per sub-pulse in a burst as well as the topography are investigated and discussed.

**Keywords** Silicon · Ultrafast laser radiation · Burst pulses · MHz burst · GHz burst · Ablation · Topography · Shielding

## 1 Introduction

The continued development of ultrafast laser sources to higher average powers [1–5] has led to so-called burst lasers in recent advances for an optimal throughput and efficiency in laser micro-machining. A burst comprises a pulse packet containing at least two and up to several hundred sub-pulses [6–10]. Within a burst, each of these sub-pulses has a high enough pulse energy to be used for laser micro-machining, while the total energy of all sub-pulses in a pulse packet together is close to the maximum available pulse energy of the laser.

In recent studies, two burst regimes have been established in terms of providing maximum ablation efficiency and optimal surface quality. The first regime is the so-called MHz burst with sub-pulse repetition times in the nanosecond range. A comparably high efficiency to conventional pulsed laser radiation was demonstrated on stainless steel [11, 12], cemented tungsten carbide [13] and metallic implant material [14], however with a significantly higher throughput. The efficiency is even increased on copper [11, 13, 15, 16]

and silicon [16, 17]. Furthermore, in this regime, a good surface roughness is realized at a certain number of sub-pulses, which is comparable to values using nanosecond pulses [18]. As soon as the number of sub-pulses is higher as the optimal range, the surface quality decreases due to increasing roughness values [19, 20]. Furthermore, using MHz burst pulses, an iterative shielding of the laser radiation by an existing ablation cloud was demonstrated, depending on the number of sub-pulses [13, 21, 22].

The second regime is the so-called GHz burst with sub-pulse repetition times in the picosecond range. Using GHz burst pulses with pulse energies per sub-pulse below the ablation threshold of the non-burst regime resulted in significant increases of the efficiency even with a small number of sub-pulses on glasses [23, 24]. Similar results were obtained for stainless steel, copper, aluminium and silicon, but in this case several hundred sub-pulses are required [25, 26]. Recent studies utilizing GHz burst pulses with pulse energies per sub-pulse above the ablation threshold of the non-burst regime have been used to polish comparatively rough material surfaces produced during 3D micro-machining or milling on metals [19, 23, 27–29], cemented tungsten carbide [27] and silicon [23, 27]. In this parameter range, subsequent pulses interact with a laser-induced plasma, allowing the assumption that a thermo-mechanical smoothing of the material surface takes place as a result of plasma-induced shock waves [27, 30, 31]. However, using GHz burst pulses with sub-pulse pulse energies above the ablation threshold leads to a strong shielding of subsequent

✉ Daniel Metzner  
metzner@hs-mittweida.de

<sup>1</sup> Department of Physics and Laser Technology, University of Applied Sciences Mittweida, Technikumplatz 17, 09648 Mittweida, Germany

<sup>2</sup> Department of Materials and Surface Engineering, Chemnitz University of Technology, 09107 Chemnitz, Germany

pulses by an existing plasma cloud and reduces the ablation efficiency by up to 90 % [27, 28, 32–34].

The referenced studies obtained their results mainly from laser micro-milling, making a detailed analysis of the topography from single structures impossible due to the multiple number of bursts. The aim of this study is a detailed investigation of the ablated volume per single burst and sub-pulse as well as the resulting topography of the created cavity depending on the pulse duration and the number of sub-pulses using single MHz and GHz bursts.

## 2 Experimental setup

### 2.1 Laser processing

An amplified solid-state laser (Pharos PH1-20, Light Conversion) was used for the experiments, generating laser radiation with a maximum average power  $P_{av}$  of 20 W, a pulse repetition rate  $f_{rep}$  up to 1 MHz, an emitting wavelength  $\lambda$  of  $1028 \pm 5$  nm, and a variable pulse duration  $\tau_H$  ranging from 270 to 10 ps. The spatial intensity distributions of the laser radiation nearly equals an ideal Gaussian distribution ( $M^2 \leq 1.2$ ). A spherical lens with a focal length of 160 mm was utilized for focusing the laser radiation with a beam waist radius  $w_0$  of  $14.2 \mu\text{m}$  on the material surface, measured by a Primes MicroSpotMonitor in accordance with ISO 11146. A galvanometer scanner head was used to deflect the laser radiation across the sample surface.

In principal, the laser generated bursts with a certain number  $N$  of sub-pulses per burst from one (representing the non-burst regime) up to nine using MHz burst and up to 25 by GHz burst pulses. In this study, a maximum number of nine sub-pulses was used for immediate comparability of the results in both burst regimes. The sub-pulse repetition rate was 65 MHz and 5 GHz, which corresponds to a time delay between subsequent pulses of about 15.4 ns for MHz burst and 200 ps for GHz burst pulses, respectively.

Using a fluence  $\Phi_0$  of  $2.0 \text{ J/cm}^2$  per sub-pulse, given by

$$\Phi_0 = \left[ \frac{2 P_{av}}{\pi w_0^2 f_{rep}} = \frac{2 E_p}{\pi w_0^2} \right] \text{ J/cm}^2 \quad (1)$$

correlated to the pulse energy  $E_p$  of  $6.3 \mu\text{J}$ , separate cavities were created on a monocrystalline silicon wafer  $\langle 111 \rangle$  depending on the number of sub-pulses and on the pulse duration in both burst regimes. The selected fluence of  $2.0 \text{ J/cm}^2$  per sub-pulse is well above the single-pulse threshold fluence of  $0.7 \text{ J/cm}^2$  and in an ablation regime without hydrodynamic motion in the non-burst regime ( $N = 1$ ) during the interaction between the first sub-pulse and the material surface [35].

### 2.2 Analytical methods

The created cavities were measured using confocal laser scanning-microscopy (Olympus model Lext 3D OLS4100). Referring to Fig. 1, a zero plane was referenced to the non-irradiated material surface. Based on this referencing, a bulge volume  $V_{bulge}$  was measured above the zero plane, caused by solidified melt ejection. Furthermore, a cavity volume  $V_{cavity}$  below the zero level was measured. The ablated volume per burst  $V_{burst}(N)$  as a function of the number of sub-pulses, defined by

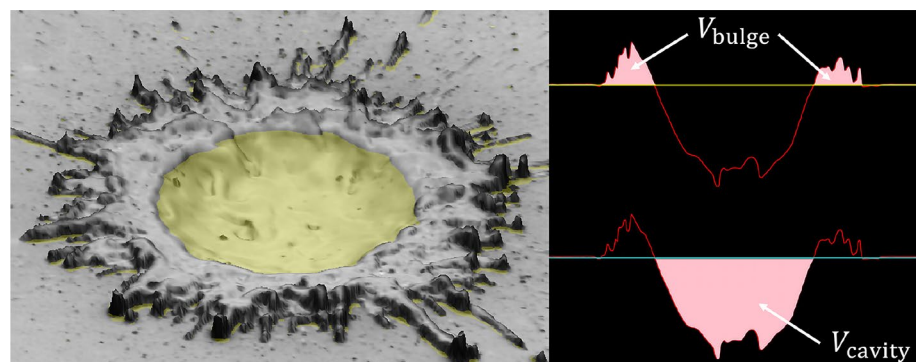
$$V_{burst}(N) = [V_{cavity}(N) - V_{bulge}(N)] \mu\text{m}^3 \quad (2)$$

results from the difference between the cavity and corresponding bulge volume. The ablated volume per sub-pulse, given by

$$V_{pulse}(N) = [V_{burst}(N) - V_{burst}(N-1)] \mu\text{m}^3 \quad (3)$$

permits an analysis of the ablation volume in terms of the part that each individual sub-pulse has contributed to the ablated burst volume [13]. Further image recordings were performed by scanning electron microscopy (SEM) (JeolJSM-6512V).

**Fig. 1** Exemplary representation of a cavity measured by confocal microscopy, the bulge  $V_{bulge}$  and the cavity volume  $V_{cavity}$  referenced to the non-irradiated material surface



### 3 Results and discussion

#### 3.1 MHz burst pulses

Using MHz burst pulses, the cavity volume (see Fig. 2 left) increases considerably according to the number of sub-pulses, going from one sub-pulse in a range of  $3 \mu\text{m}^3$  and  $9 \mu\text{m}^3$  up to a maximum of  $650 \mu\text{m}^3$  at 10 ps to  $810 \mu\text{m}^3$  at 270 fs with nine sub-pulses per burst. This non-linear increase in the cavity volume results from the accumulation of residual heat [13, 36–39], meaning that in addition to the ablation of material of each individual sub-pulse by spallation and phase explosion, the boiling temperature in the interaction zone is continuously exceeded above a certain number of sub-pulses and evaporation of material takes place [13]. In the non-burst regime, compared to a pulse duration of 10 ps, a three times increased cavity volume was measured by using 270 fs. This correlation has been demonstrated in other studies whereby the ablation threshold on silicon decreases with shorter pulses resulting in a higher amount of material being ablated for the same fluence [40–42]. In contrast to the non-burst regime, the ratio of cavity volumes between 10 ps and 270 fs is

significantly lower for MHz burst pulses, thus heat accumulation induced material removal dominates and the pulse duration has a negligible influence on the resulting cavity volume.

The accumulation of residual heat caused by MHz burst pulses leads to the generation of a melt film with depths ranging from several hundred nanometers to a few micrometers [12, 14, 43, 44]. The interaction of subsequent sub-pulses with this melt film permits melt to be ejected from the interaction zone, resulting in a bulge volume. Referring to Fig. 2 (middle), a bulge volume of  $2 \mu\text{m}^3$  was measured using a burst containing two sub-pulses at a pulse duration of 10 ps. With an increase in the number of sub-pulses, the bulge volume increases continuously up to a value of  $500 \mu\text{m}^3$  with nine sub-pulses. Compared to the corresponding cavity volume (Fig. 2 left), the progression of the graph is similar to the bulge volume. Consequently, the resulting cavity volume is mainly generated by the ejection of melt. In Fig. 3b, the topography of the generated cavities visualises this conclusion by means of SEM images. Thereby, by increasing the number of sub-pulses referring to the piston effect [45–48], increasingly more melt is pushed out and solidifies near the edge of the cavity.

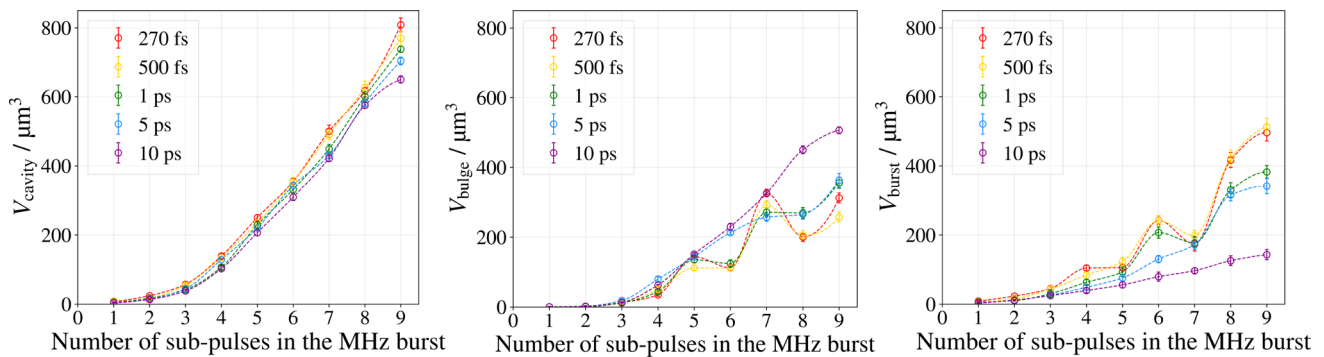


**Fig. 2** Ablation volume per burst  $V_{\text{burst}}$ , determined from the cavity volume  $V_{\text{cavity}}$  and bulge volume  $V_{\text{bulge}}$  as a function of the number of sub-pulses and of the pulse duration from 270 fs up to 10 ps. The values are interpolated with a cubic spline function to guide the eye

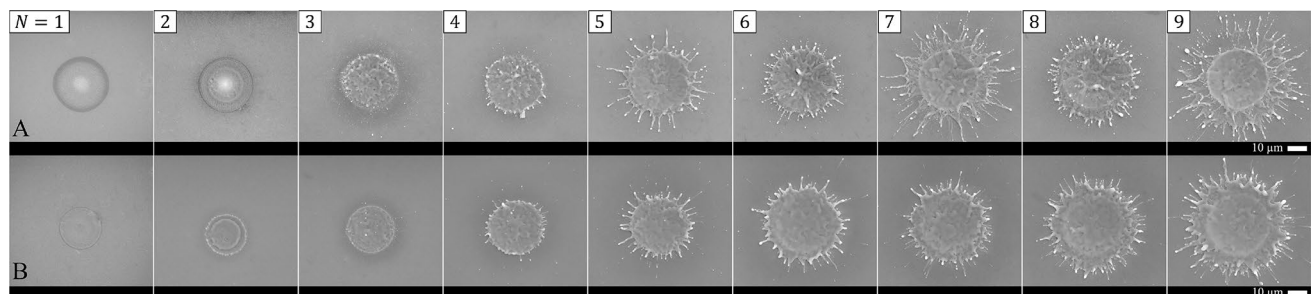


**Fig. 3** Cavities on silicon, generated from a MHz burst pulses with a fluence per sub-pulse of  $2.0 \text{ J/cm}^2$  in dependence on the number of sub-pulses  $N$  and with a pulse duration of **a** 270 fs and **b** 10 ps

In the case of 1 ps and shorter pulse durations, an iterative decrease and increase of the bulge volume is noticeable starting at five sub-pulses (Fig. 2 middle). Furthermore, the amplitude of the iteration increases with shorter pulse durations.

The increased bulge volume at five, seven and nine sub-pulses per burst and the reduced bulge volume using six and eight sub-pulses is similarly illustrated by the resulting topography of the generated cavities in Fig. 3a by means of SEM images. Compared to the generated cavities using a pulse duration of 10 ps (Fig. 3b), whereby the melt ejection solidified near the edge of the cavity, the melt is ejected very widely from the interaction zone at 270 fs in the case of five, seven and nine sub-pulses. The topography of the solidified melt ejection of bursts with four, six and eight sub-pulses is comparable to the topography of the solidified melt ejection of bursts with a pulse duration of 10 ps. This phenomenon could be attributed to the assumption that the interaction of sub-pulses with an existing ablation cloud influences the melting dynamics in the cavity. The initial travel velocity of ablated particles under atmospheric pressure is in the range of a few 100 m/s [21, 49–53]. Consequently, using burst pulses with sub-pulse repetition times in the nanosecond range, the ablated particles are propagated to a distance of a few micrometers from the material surface forming a dense ablation cloud. The pulse energy of subsequent sub-pulses is fully or partially absorbed, resulting in ablated material forced back to the surface [13, 21, 38, 52, 54]. The induced pressure from redeposited particles on the material surface can be significantly higher compared to a direct interaction of ultrafast laser radiation without re-deposition [55]. In conclusion, in the case of a strong re-deposition of ablated material, it can be assumed that considerably more melt is ejected from the cavity. However, a fundamental explanation of these fluid dynamics is not state of the art.

The ablated volume per burst  $V_{\text{burst}}$  results from the difference of the cavity volume and the corresponding volume of the solidified melt ejection (see Sect. 2.2, Eq. 2). Using MHz burst pulses and a pulse duration of 10 ps, the ablation volume per burst, presented in Fig. 2 (right), increases continuously up to a value of  $145 \mu\text{m}^3$  by nine sub-pulses. The iterative increase or decrease of the bulge volume transmits to the ablation volume per burst from a pulse duration of 5 ps and shorter, leading to a comparably low ablation volume per burst for five and seven sub-pulses and a high ablation volume per burst for six and eight sub-pulses. This oscillating trend has also been demonstrated in other studies on copper [10, 21, 22], brass [16], aluminium [34] and stainless steel [12], starts on metals from the second sub-pulse onwards, resulting in a decrease in the removal volume per burst with an even number of sub-pulses and an increase with an odd number. In context of the referenced studies, the oscillation of the

ablation volume per burst (Fig. 2, right) can be explained as follows: the fifth sub-pulse is fully or partially shielded by ablated particles, but its energy clears the ablation cloud such that the sixth sub-pulse can be absorbed onto the surface. The sixth sub-pulse again produces an ablation cloud, and the seventh sub-pulse is therefore shielded and so on. The difference in the initial start point of the iterative change in the ablation volume between the state of the art and this study can be explained by considering that previous results were generated exclusively by multi-burst plane ablations and not by single MHz burst pulses. In conclusion, multi-burst incubation effects possibly influence the initial start point of the iteration. Furthermore, no evaluation can be made from the results of multi-burst surface ablation on the basis of the solidified melt ejection, due to the influence and relativization of subsequent bursts.

Based on the determined ablation volumes per burst  $V_{\text{burst}}$ , the ablated volume per sub-pulse  $V_{\text{pulse}}$  was calculated and the results are illustrated in Fig. 4. The values indicate a continuous increase of the ablation volume up to the fourth sub-pulse, with an increase of the volume per sub-pulse leading to shorter pulse durations.

Starting with the fourth and further even-numbered sub-pulses, the pulse energy is used primarily for ablating material due to the high ablation volume of up to  $250 \mu\text{m}^3$ . In comparison, considerably less material is ablated with odd sub-pulses. Based on the measured bulge volume (Fig. 2, middle), in this case molten material is mainly ejected from the cavity (Fig. 3a). The negative values for the seventh sub-pulse and pulse durations of less than or equal to 1 ps may suggest in addition to the pronounced ejection of melt, that more material was redeposited in the cavity than ablated.

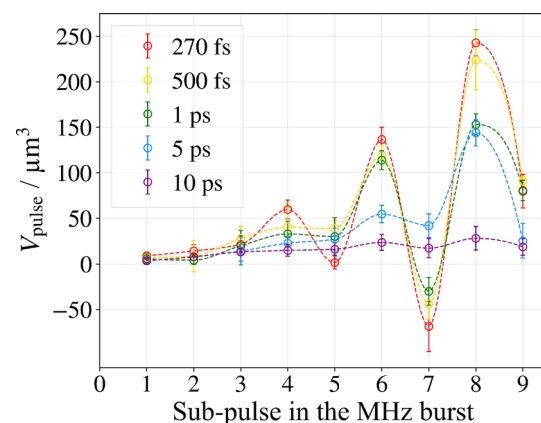
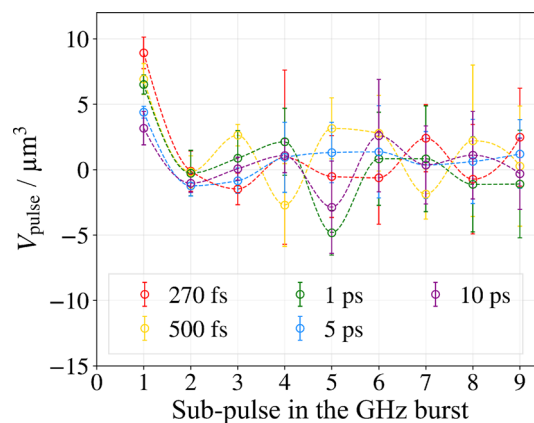


Fig. 4 Ablation volume per sub-pulse  $V_{\text{pulse}}$  in the MHz burst as a function of the pulse duration from 270 fs up to 10 ps. The values are interpolated with a cubic spline function to guide the eye

### 3.2 GHz burst pulses

In the investigated parameter range, a cavity volume of up to  $9 \mu\text{m}^3$  was measured for GHz burst pulses with one sub-pulse and a maximum cavity volume of approximately  $60 \mu\text{m}^3$  using nine sub-pulses (Fig. 5 left). The near-linear increase of the cavity volume with the number of sub-pulses indicates that, in contrast to MHz burst pulses, the accumulation of residual heat is not contributing to the resulting cavity volume.

The values of the measured bulge volume illustrated in Fig. 5 (middle) indicate an almost identical shape of the characteristic graph in comparison to the cavity volume for all investigated pulse durations. In conclusion, for GHz burst pulses, material was primarily melted and less ablated. The ablation volume per burst presented in Fig. 5 (right) demonstrates this point, indicating that no additional material was ablated by increasing the number of sub-pulses compared to the first sub-pulse. In contrast to the shielding of laser radiation using MHz burst pulses, However, the physical effects that can lead to shielding are different for temporal sub-pulse delays of a few picoseconds from those in the nanosecond range. During the interaction of ultrafast laser radiation with matter, two pressure waves are generated and propagate from the surface into the bulk. The first shock wave leads locally to a compression of material and the subsequent rarefaction wave leads to a dilution [51, 54, 56, 57]. The resulting negative stresses by a sufficiently intense rarefaction wave induces a layer-wise fragmentation of material. For sub-pulse repetition times up to a few 100 ps, rarefaction wave interference takes place [34, 51]. The destructive interference weakens the rarefaction waves to reduce the resulting stress and less material is ablated. If the time delay is further extended up to a few nanoseconds, subsequent sub-pulses interact with material that has lifted off the surface so that no physical connection and interference of subsequent rarefaction waves occurs [51, 58]. The ablated material forms an ablation cloud that shields the laser radiation of subsequent



**Fig. 6** Ablation volume per sub-pulse  $V_{\text{pulse}}$  in the GHz burst as a function of the pulse duration from 270 fs up to 10 ps. The values are interpolated with a cubic spline function to guide the eye

sub-pulses, leading to an increase in the temperature of the ablation cloud and to plasma formation [23, 27, 32, 34, 39, 52, 59]. Based on the calculated ablation volumes per sub-pulse of a GHz burst (Fig. 6), the strong shielding by an existing ablation cloud or plasma is verified. The first sub-pulse ablates a volume of up to  $9 \mu\text{m}^3$  creating an ablation cloud. From the second sub-pulse on, considering the error deviations, no further material is ablated.

In Fig. 7, SEM images visualise the generated cavities using GHz burst pulses at a pulse duration of 270 fs depending on the number of sub-pulses. Compared to the resulting topography using MHz burst pulses, which is mainly characterized by melt ejection out of the cavity, the resulting topography using GHz burst pulses differs significantly. Generally, starting with two sub-pulses, a solidified melt front was formed at the edge of the cavity, as illustrated in Fig. 8 by means of depth profiles, increasing with a higher number of sub-pulses. Furthermore, rotationally symmetrical wave profiles with a depth of up to 150 nm were formed around the cavity centre. Two assumptions can be

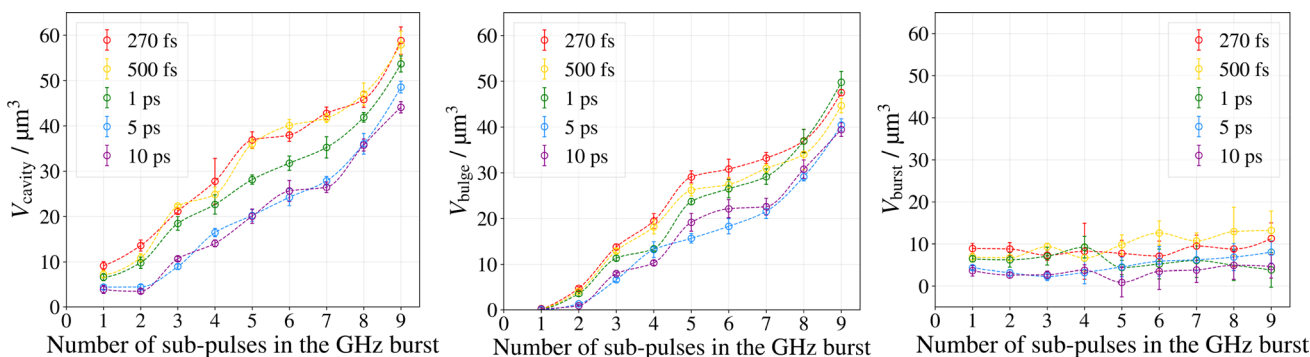


**Fig. 5** Ablation volume per GHz burst  $V_{\text{burst}}$ , determined from the cavity volume  $V_{\text{cavity}}$  and bulge volume  $V_{\text{bulge}}$  as a function of the number of sub-pulses and of the pulse duration from 270 fs up to 10 ps. The values are interpolated with a cubic spline function to guide the eye

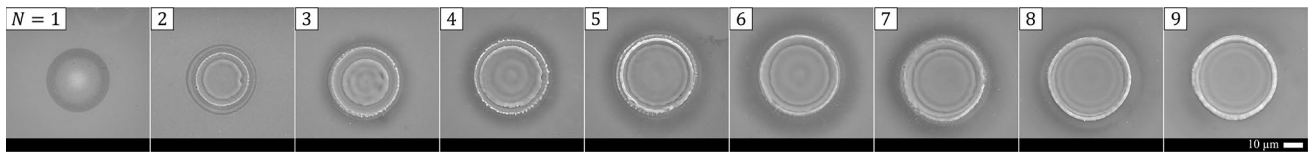


**Fig. 7** Cavities on silicon, generated from single GHz burst pulses with a fluence per sub-pulse of  $2.0 \text{ J/cm}^2$  in dependence on the number of sub-pulses  $N$  using a pulse duration of 270 fs

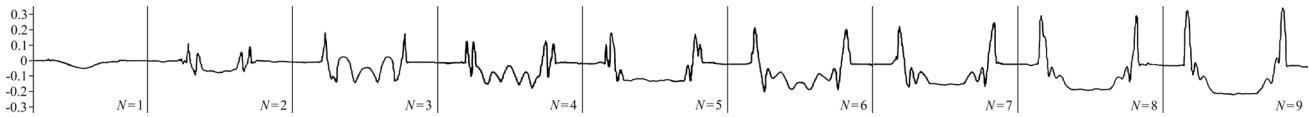


**Fig. 8** Depth profile of the cavities (measured with confocal laser-scanning microscopy), generated by single GHz burst pulses with a fluence per sub-pulse of  $2.0 \text{ J/cm}^2$  and a pulse duration of 270 fs in dependence on the number of sub-pulses  $N$

considered for the formation of these wave profiles: The first assumption is based on the interaction of an existing plasma and subsequent sub-pulses, thus the plasma is pumped and induces periodic shock waves given by the sub-pulse repetition time. The shock waves press melt wavelike from the centre to the edge of the cavity. This would account for the continuous increase in the solidified outer melt front with an increase in the number of sub-pulses. The second assumption based on the generation of an expanding highly dynamic plasma and the resulting formation and evolution of a sub-surface melt front [60–62]. In this case, an interference by reflected laser radiation occurs at the front and back side of the layer, detectable as Newton rings and characterize the melt front evolution. In this context, supersonic velocities of the Newton rings up to Mach number 6 and high-pressure shock waves nearly 30 GPa were determined using femto-second pulses [61, 63]. The results of previous studies were obtained from experiments with single pulses, thus the influence of multiple sub-pulses in a GHz burst on the resulting ring patterns is not state of the art.

## 4 Conclusions

The dependence on the number of sub-pulses per burst of the resulting ablation volume and topography were investigated by ablating silicon with ultrafast laser radiation emitting a wavelength of 1030 nm with pulse durations of 270 fs up to 10 ps using single MHz and GHz burst pulses.

Using MHz burst pulses, the cavity volume increased from up to  $9 \mu\text{m}^3$  for one sub-pulse to a maximum of  $810 \mu\text{m}^3$  for nine sub-pulses. This significant increase in the cavity volume was explained by the accumulation of residual heat. In contrast to the non-burst regime, represented by one sub-pulse in the burst, the cavity volume in the investigated parameter range is approximately independent of the pulse

duration. The melt dynamics and the ejection of the melt from the cavity resulted in a solidified bulge volume depending on the pulse duration and the number of sub-pulses. Based on the ablation volume per sub-pulse, it was demonstrated that primarily with odd sub-pulses comparatively less material was ablated, whereas more melt was ejected out of the cavity.

The results obtained for GHz burst pulses revealed close to a linear increase in the cavity and a comparable trend in the bulge volume with increased sub-pulses. The ablation volumes per sub-pulse indicated from the second sub-pulse in the GHz burst onwards in general that no material was ablated and therefore a strong shielding of the laser radiation by a given ablation cloud and plasma takes place. Furthermore, SEM images and depth profiles demonstrated ring patterns within the cavity with a solidified melt front at the edge of the cavity.

The primary findings of this study are related to the strong dependence of the fluid and thermo-mechanical dynamics during the interaction of multiple burst pulses on the sub-pulse repetition time, which will be fundamentally investigated in subsequent studies using time-resolved experiments and simulations.

**Acknowledgements** This study was funded by the Deutsche Forschungsgemeinschaft (DFG, German Research Foundation)—458053570.

Funded by  
**DFG** Deutsche  
 Forschungsgemeinschaft  
 German Research Foundation

**Author Contributions** The authors declare that they have no known competing financial interests or personal relationships that could have appeared to influence the work reported in this paper.

**Funding** Open Access funding enabled and organized by Projekt DEAL.

**Open Access** This article is licensed under a Creative Commons Attribution 4.0 International License, which permits use, sharing, adaptation, distribution and reproduction in any medium or format, as long as you give appropriate credit to the original author(s) and the source, provide a link to the Creative Commons licence, and indicate if changes were made. The images or other third party material in this article are included in the article's Creative Commons licence, unless indicated otherwise in a credit line to the material. If material is not included in the article's Creative Commons licence and your intended use is not permitted by statutory regulation or exceeds the permitted use, you will need to obtain permission directly from the copyright holder. To view a copy of this licence, visit <http://creativecommons.org/licenses/by/4.0/>.

## References

- P. Russbuedt, T. Mans, J. Weitenberg, H.D. Hoffmann, R. Poprawe, *Opt. Lett.* **35**(24), 4169 (2010). <https://doi.org/10.1364/OL.35.004169>
- T. Nubbemeyer, M. Kaumanns, M. Ueffing, M. Gorjan, A. Alismail, H. Fattahi, J. Brons, O. Pronin, H.G. Barros, Z. Major et al., *Opt. Lett.* **42**(7), 1381 (2017). <https://doi.org/10.1364/OL.42.001381>
- C. Gaida, M. Gebhardt, T. Heuermann, F. Stutzki, C. Jauregui, J. Limpert, *Opt. Lett.* **43**(23), 5853 (2018). <https://doi.org/10.1364/OL.43.005853>
- T. Dietz, M. Jenne, D. Bauer, M. Scharun, D. Sutter, A. Killi, *Opt. Express* **28**(8), 11415 (2020). <https://doi.org/10.1364/OE.383926>
- M. Müller, M. Kienel, A. Klenke, T. Gottschall, E. Shestaeve, M. Plötner, J. Limpert, A. Tünnermann, arXiv preprint (2021). <https://doi.org/10.1364/OL.41.003439>. arXiv:2101.08498
- A. Semerok, C. Dutouquet, *Thin Solid Films* **453**, 501 (2004). <https://doi.org/10.1016/j.tsf.2003.11.115>
- J. Hernandez-Rueda, J. Siegel, M. Galvan-Sosa, A.R. de la Cruz, J. Solis, *JOSA B* **30**(5), 1352 (2013). <https://doi.org/10.1364/JOSAB.30.001352>
- G. Bonamis, K. Mishchik, J. Lopez, I. Manek-Hönninger, E. Audouard, C. Honninger, E. Mottay, in *CLEO: Applications and Technology* (Optical Society of America, 2018), p. AM2M-4. [https://doi.org/10.1364/CLEO\\_AT.2018.AM2M.4](https://doi.org/10.1364/CLEO_AT.2018.AM2M.4)
- J. Mur, R. Petkovšek, *Appl. Phys. A* **124**(1), 1 (2018). <https://doi.org/10.1007/s00339-017-1490-4>
- A. Žemaitis, M. Gaidys, P. Gečys, M. Barkauskas, M. Gedvilas, *Opt. Express* **29**(5), 7641 (2021). <https://doi.org/10.1364/OE.417883>
- B. Neuenschwander, T. Kramer, B. Lauer, B. Jaeggi, in *Laser Applications in Microelectronic and Optoelectronic Manufacturing (LAMOM) XX*, vol. 9350 (International Society for Optics and Photonics, 2015), p. 93500U. <https://doi.org/10.1117/12.2076455>
- P. Lickschat, D. Metzner, S. Weißmantel, *J. Laser Appl.* **33**(2), 022005 (2021). <https://doi.org/10.2351/7.0000271>
- D. Metzner, P. Lickschat, S. Weißmantel, *Appl. Phys. A* **125**(7), 1 (2019). <https://doi.org/10.1007/s00339-019-2755-x>
- D. Metzner, P. Lickschat, S. Weißmantel, *Appl. Phys. A* **126**(2), 1 (2020). <https://doi.org/10.1007/s00339-019-3203-7>
- T. Kramer, Y. Zhang, S. Remund, B. Jaeggi, A. Michalowski, L. Grad, B. Neuenschwander, *J. Laser Micro Nanoeng.* **12**(2), 107 (2017). <https://doi.org/10.2961/jlmm.2017.02.0011>
- N. Hodgson, H. Allegre, A. Caprara, A. Starodoumov, S. Betten-court, in *Frontiers in Ultrafast Optics: Biomedical, Scientific, and Industrial Applications XXI*, vol. 11676 (International Society for Optics and Photonics, 2021), p. 116760G. <https://doi.org/10.1117/12.2576277>
- F. Caballero-Lucas, K. Obata, K. Sugioka, *Int. J. Extreme Manuf.* **4**(1), 015103 (2022). <https://doi.org/10.1088/2631-7990/ac466e/meta>
- M. Domke, V. Matylitsky, S. Stroj, *Appl. Surf. Sci.* **505**, 144594 (2020). <https://doi.org/10.1016/j.apsusc.2019.144594>
- D. Metzner, P. Lickschat, S. Weißmantel, *J. Laser Appl.* **33**(1), 012057 (2021). <https://doi.org/10.2351/7.0000352>
- D. Metzner, P. Lickschat, S. Weißmantel, *Appl. Phys. A* **127**(1), 1 (2021). <https://doi.org/10.1007/s00339-020-04179-w>
- D.J. Förster, S. Faas, S. Gröniger, F. Bauer, A. Michalowski, R. Weber, T. Graf, *Appl. Surf. Sci.* **440**, 926 (2018). <https://doi.org/10.1016/j.apsusc.2018.01.297>
- B. Bornschlegel, J. Finger, *J. Laser Micro Nanoeng.* **14**(1), 88 (2019). <https://doi.org/10.2961/jlmm.2019.01.0015>
- S.M. Remund, M. Gafner, M.V. Chaja, A. Urniezius, S. Butkus, B. Neuenschwander, *Procedia CIRP* **94**, 850 (2020). <https://doi.org/10.1016/j.procir.2020.09.111>
- S. Schwarz, S. Rung, C. Esen, R. Hellmann, *Opt. Lett.* **46**(2), 282 (2021). <https://doi.org/10.1364/OL.415959>
- G. Bonamis, K. Mishchik, E. Audouard, C. Hönninger, E. Mottay, J. Lopez, I. Manek-Hönninger, *J. Laser Appl.* **31**(2), 022205 (2019). <https://doi.org/10.2351/1.5096087>
- G. Bonamis, E. Audouard, C. Hönninger, J. Lopez, K. Mishchik, E. Mottay, I. Manek-Hönninger, *Opt. Express* **28**(19), 27702 (2020). <https://doi.org/10.1364/OE.400624>
- D. Metzner, P. Lickschat, S. Weißmantel, *Appl. Surf. Sci.* **531**, 147270 (2020). <https://doi.org/10.1016/j.apsusc.2020.147270>
- K. Obata, F. Caballero-Lucas, K. Sugioka, *J. Laser Micro Nanoeng.* **16**(1), 19 (2021). <https://doi.org/10.2961/jlmm.2021.01.2004>
- P. Lickschat, D. Metzner, S. Weißmantel, *J. Laser Appl.* **33**(4), 042002 (2021). <https://doi.org/10.2351/7.0000437>
- O.A. Ranjbar, Z. Lin, A.N. Volkov, *Vacuum* **157**, 361 (2018). <https://doi.org/10.1016/j.vacuum.2018.08.065>
- S. Butkus, V. Jukna, D. Paipulas, M. Barkauskas, V. Sirutkaitis, *Micromachines* **11**(8), 733 (2020). <https://doi.org/10.3390/mi11080733>
- T. Hirsiger, M. Gafner, S. Remund, M.V. Chaja, A. Urniezius, S. Butkus, B. Neuenschwander, in *Laser Applications in Microelectronic and Optoelectronic Manufacturing (LAMOM) XXV*, vol. 11267 (International Society for Optics and Photonics, 2020), p. 112670T. <https://doi.org/10.1117/12.2543948>
- O. Balachninaite, V. Tamulienė, L. Eičas, V. Vaičiaitis, *Results Phys.* **22**, 103847 (2021). <https://doi.org/10.1016/j.rinp.2021.103847>
- D.J. Förster, B. Jäggi, A. Michalowski, B. Neuenschwander, *Materials* **14**(12), 3331 (2021). <https://doi.org/10.3390/ma14123331>
- R. Moser, M. Domke, J. Winter, H.P. Huber, G. Marowsky, *Adv. Opt. Technol.* **7**(4), 255 (2018). <https://doi.org/10.1515/aot-2018-0013>
- R. Weber, T. Graf, P. Berger, V. Onuseit, M. Wiedenmann, C. Freitag, A. Feuer, *Opt. Express* **22**(9), 11312 (2014). <https://doi.org/10.1364/OE.22.011312>
- F. Bauer, A. Michalowski, T. Kiedrowski, S. Nolte, *Opt. Express* **23**(2), 1035 (2015). <https://doi.org/10.1364/OE.23.001035>
- B. Neuenschwander, B. Jaeggi, D.J. Foerster, T. Kramer, S. Remund, *J. Laser Appl.* **31**(2), 022203 (2019). <https://doi.org/10.2351/1.5096083>

39. N. Hodgson, H. Allegre, A. Starodoumov, S. Bettencourt, J. Laser Micro/Nanoeng. (2020). <https://doi.org/10.2961/jlmn.2020.03.2014>
40. D. Zayarny, A. Ionin, S. Kudryashov, S. Makarov, A. Kuchmizhak, O. Vitrik, Y.N. Kulchin, JETP Lett. **103**(12), 752 (2016). <https://doi.org/10.1134/S0021364016120158>
41. I. Saraeva, S. Kudryashov, A. Rudenko, M. Zhilnikova, D. Ivanov, D. Zayarny, A. Simakin, A. Ionin, M. Garcia, Appl. Surf. Sci. **470**, 1018 (2019). <https://doi.org/10.1016/j.apsusc.2018.11.199>
42. N. Smirnov, S. Kudryashov, P. Danilov, A. Nastulyavichus, A. Rudenko, A. Ionin, Appl. Surf. Sci. (2019). <https://doi.org/10.1016/j.apsusc.2019.03.100>
43. M. Osbild, A. Brenner, L. Röther, J. Finger, Procedia CIRP **94**, 936 (2020). <https://doi.org/10.1016/j.procir.2020.09.094>
44. A. Brenner, L. Röther, M. Osbild, J. Finger, in *Laser-based Micro- and Nanoprocessing XIV*, vol. 11268 (International Society for Optics and Photonics, 2020), p. 112680P. <https://doi.org/10.1117/12.2551481>
45. A. Ruf, D. Breitling, P. Berger, F. Dausinger, H. Huegel, in *Third International Symposium on Laser Precision Microfabrication*, vol. 4830 (International Society for Optics and Photonics, 2003), pp. 73–78. <https://doi.org/10.1117/12.486555>
46. N. Stojanovic, D. Von Der Linde, K. Sokolowski-Tinten, U. Zastrau, F. Perner, E. Förster, R. Sobierajski, R. Nietubyc, M. Jurek, D. Klinger et al., Appl. Phys. Lett. **89**(24), 241909 (2006). <https://doi.org/10.1063/1.2405398>
47. M. Stafe, J. Appl. Phys. **112**(12), 123112 (2012). <https://doi.org/10.1063/1.4771692>
48. K.S. Singh, A.K. Sharma, J. Appl. Phys. **119**(18), 183301 (2016). <https://doi.org/10.1063/1.4948950>
49. J.F. Düsing, D.J. Hwang, C.P. Grigoropoulos, A. Ostendorf, R. Kling, in *International Congress on Applications of Lasers and Electro-Optics*, vol. 2009 (Laser Institute of America, 2009), pp. 888–892. <https://doi.org/10.2351/1.5061659>
50. C. Wu, L.V. Zhigilei, Appl. Phys. A **114**(1), 11 (2014). <https://doi.org/10.1007/s00339-013-8086-4>
51. M.E. Povarnitsyn, V.B. Fokin, P.R. Levashov, T.E. Itina, Phys. Rev. B **92**(17), 174104 (2015). <https://doi.org/10.1103/PhysRevB.92.174104>
52. A.A. Foumani, D.J. Förster, H. Ghorbanfekr, R. Weber, T. Graf, A.R. Niknam, Appl. Surf. Sci. **537**, 147775 (2021). <https://doi.org/10.1016/j.apsusc.2020.147775>
53. T.V. Kononenko, D.N. Sovyk, V.V. Kononenko, V.I. Konov, Opt. Laser Technol. **150**, 107921 (2022). <https://doi.org/10.1016/j.optlastec.2022.107921>
54. M. Spellauge, J. Winter, S. Rapp, C. McDonnell, F. Sotier, M. Schmidt, H.P. Huber, Appl. Surf. Sci. **545**, 148930 (2021). <https://doi.org/10.1016/j.apsusc.2021.148930>
55. D.J. Förster, S. Faas, R. Weber, T. Graf, Appl. Surf. Sci. **510**, 145391 (2020). <https://doi.org/10.1016/j.apsusc.2020.148472>
56. N.M. Bulgakova, I.M. Bourakov, N.A. Bulgakova, Phys. Rev. E **63**(4), 046311 (2001). <https://doi.org/10.1103/PhysRevE.63.046311>
57. V. Mazhukin, M. Demin, A. Shapranov, Appl. Surf. Sci. **302**, 6 (2014). <https://doi.org/10.1016/j.apsusc.2014.01.111>
58. M. Povarnitsyn, T. Itina, K. Khishchenko, P. Levashov, Phys. Rev. Lett. **103**(19), 195002 (2009). <https://doi.org/10.1103/PhysRevLett.103.195002>
59. S.I. Kudryashov, A.A. Samokhvalov, Y.D. Golubev, D.S. Ivanov, M.E. Garcia, V.P. Veiko, B. Rethfeld, V.Y. Mikhailovskii, Appl. Surf. Sci. **537**, 147940 (2021). <https://doi.org/10.1016/j.apsusc.2020.147940>
60. D. von der Linde, K. Sokolowski-Tinten, in *ICONO'98: Fundamental Aspects of Laser-Matter Interaction and New Nonlinear Optical Materials and Physics of Low-Dimensional Structures*, vol. 3734 (International Society for Optics and Photonics, 1999), pp. 2–9. [https://doi.org/10.1016/S0169-4332\(99\)00440-7](https://doi.org/10.1016/S0169-4332(99)00440-7)
61. I. Carrasco-García, J.M. Vadiello, J.J. Laserna, Spectrochim. Acta Part B **131**, 1 (2017). <https://doi.org/10.1016/j.sab.2017.02.014>
62. N. Bykovskii, Y.V. Senatskii, Phys. Solid State **60**(2), 404 (2018). <https://doi.org/10.1134/S1063783418020087>
63. T. Pezeril, G. Saini, D. Veysset, S. Kooi, P. Fidkowski, R. Radovitzky, K.A. Nelson, Phys. Rev. Lett. **106**(21), 214503 (2011). <https://doi.org/10.1103/PhysRevLett.106.214503>